1 # Influence of urban spatial configuration and sea breeze on land surface temperature on

2 # summer clear-sky days

3

4 **Yuhei Yamamoto[1]**

5 Affiliation: [1]Disaster Prevention Research Institute, Kyoto University, Uji, Kyoto 611-0011 Japan.

6 E-mail: yamamoto_y@storm.dpri.kyoto-u.ac.jp

7 **Hirohiko Ishikawa[1]**

8 Affiliation: [1]Disaster Prevention Research Institute, Kyoto University, Uji, Kyoto 611-0011 Japan.

9 E-mail: ishikawa@storm.dpri.kyoto-u.ac.jp

10

11 **Corresponding author: Yuhei Yamamoto**

12 *Present address: Center for Environmental Remote Sensing, Chiba University, 1-33 Yayoi-cho, Inage-ku, Chiba-

13 shi, Japan.

14

15 **Abstract**

16   Understanding the spatiotemporal characteristics of land surface temperature (LST), a physical quantity that

17 greatly contributes to the formation of urban thermal environment, is essential for constructing a sustainable urban

18 environment. This study explores the relationship between urban space, atmospheric conditions, and diurnal change

19 characteristics of LST on summer clear-sky days in an urban area of Osaka Plain using a 10 min LST dataset retrieved

20 from the Japanese geostationary satellite (Himawari-8) data. The principal temporal change patterns forming the

21 diurnal cycle of LST were extracted through a principal component analysis, and their spatial variabilities were

22 investigated through the exploitation of ground-based meteorological observation and land-use data. The result

23 showed two temporal change patterns, identified as the amplitude and phase of the diurnal change, being extracted

24 in different clear-sky days. A hierarchical cluster analysis confirmed that the spatial variations of such patterns

25 corresponded to the sea breeze and urban land-use. Moreover, LST change at daytime was found to be larger in the

26 high-density areas rather than in the low-density areas of low buildings, thereby suggesting the influence of building

27 density on LST at daytime.

28

30

31   **1. Introduction**

32   Urban heat island which is characterized by deterioration of a hot environment on an urban scale, has recently

33   become an increasingly serious phenomenon, in addition to the rise in temperature due to global warming (e.g.,

34   Kusaka et al., 2012). The foreseeable impact of urban heat islands is exemplified by the case of the Japanese

35   metropolitan areas, where approximately 50,000 heat-stroke patients are being sent to hospitals via ambulance yearly,

36   with a particularly high number of 90,000 during the summer of 2018 (Japan Fire and Disaster Management Agency,

37   2018). In addition to this direct effect, the drop in pressure accompanying the temperature rise may cause enhanced

38   precipitation (Seino et al., 2018) and retention of air pollutants, such as NOx and SOx, in the environment (Saitoh et

39   al., 1996).

40   Thermal indices have been proposed for evaluating the thermal environment in an urban area, with such examples

41   as wet-bulb globe temperature and universal thermal climate index, that consider various meteorological elements

42   i.e., surface air temperature (SAT), radiant heat, humidity, and wind speed (Budd, 2008; Jendritzky et al., 2012). SAT

43   and land surface temperature (LST) are likewise effective in evaluating the intensity of urban heat island and in

44   obtaining a detailed spatiotemporal characteristic of the thermal environment (Memon et al., 2009). SAT and LST

45   exhibit different spatiotemporal dynamics because the involved processes are dissimilar. SAT is generally observed

46   in ground weather stations. In urban areas with available dense observation networks, the spatial variability

47   characteristics of diurnal and seasonal changes of SAT have been investigated through a multivariate analysis (Kim

48   and Beik, 2005; Suzuki and Iizuka, 2009; Oku and Masumoto, 2014).

49   On the other hand, LST is retrieved by polar-orbiting satellite/aircraft sensors owing to their high spatial resolution

50   (Memon et al., 2009; Weng, 2009). The obtained LST data have been used to investigate their relationships with

51   urban vegetation and land use. Vegetation-wise, the focus is on changes in the LST from the increase/decrease of

52   green space (Li et al., 2009; Tsunematsu et al., 2016; Honjo et al., 2017), along with the vegetation phenology (Li et

53   al., 2011; Xu et al., 2013). Vegetation status is represented by vegetation coverage based on land use and land cover

54   (LULC) or remotely sensed vegetation indices, such as the normalized difference vegetation index (NDVI) and

55   fractional vegetation cover. Numerous studies have confirmed the negative relationship between LST and the

56   vegetation indices (Weng, 2009).

57   Land-use-wise, the focus is on correlations between LST and landscape metrics quantifying the horizontal urban

58   structures (Li et al., 2011; Connors et al., 2013). The metrics measure density, shape complexity, diversity, and

59   adjacency, among others, in LULC types. Additionally, relationships between LST and vertical urban structures were

60   also assessed using land-use data which have building height information (Li et al., 2011; Tsunematsu et al., 2016).

61   These studies revealed that both the cover composition and spatial configuration of the urban land surface affect the

62   LST. Yamamoto and Ishikawa (2018a) reported that the LST in coastal cities may be affected by the sea/land breeze

63   (i.e., a local meteorological field with diurnal cycle); thus, they stressed the inclusion of local meteorological effects

64   when studying the influence of urban spatial configuration on LST. In the evaluation of thermal environment using

65   instantaneous LST values obtained by polar-orbiting satellite/aircraft observations, the influences of the local

66   meteorological field on LST may pose a challenge.

67   This study presents LST observations in an urban area, through Himawari-8, a Japanese third-generation

68   geostationary satellite that can retrieve LST with high spatial (approximately 2 km) and temporal (10 min) resolutions.

69   Yamamoto and Ishikawa (2018a) attempted to apply the Himawari-8 LST product to an urban area and confirmed

70   that its spatial and temporal resolutions are effective in obtaining the thermal characteristics of land use and local

71   meteorological field in that area. Such advantage, especially temporal resolution, was utilized by this research to

72   understand the influence of urban spatial configuration and sea breeze on the temporal changes of LST during the

73   summer clear-sky days in an urban area within Osaka Plain, Japan.

74

75   **2. Data and method**

76   **2.1 Analyzed area and data**

77   Fig. 1 shows the urban study area of Osaka Prefecture, which is known to have the respective lowest and highest

78   ratios of forest and habitable areas (the latter is calculated by subtracting the area of forests, grasslands, and bodies

79   of water from the total area of the prefecture) in Japan prefectures (Japan Statistics Bureau, 2019). Additionally, the

80   prefecture has the largest number of heat-stroke patients sent to hospitals via ambulance in recent years (Japan Fire

81   and Disaster Management Agency, 2018). From the land use map in Fig. 1, there is a bay (Osaka Bay) on the west

82   side of the analyzed area. The central urban area is occupied by high buildings, and the surrounding areas are occupied

83   by low buildings (high or low density).

84   LST was retrieved by a nonlinear three-band algorithm (Yamamoto et al., 2018). The algorithm requires brightness
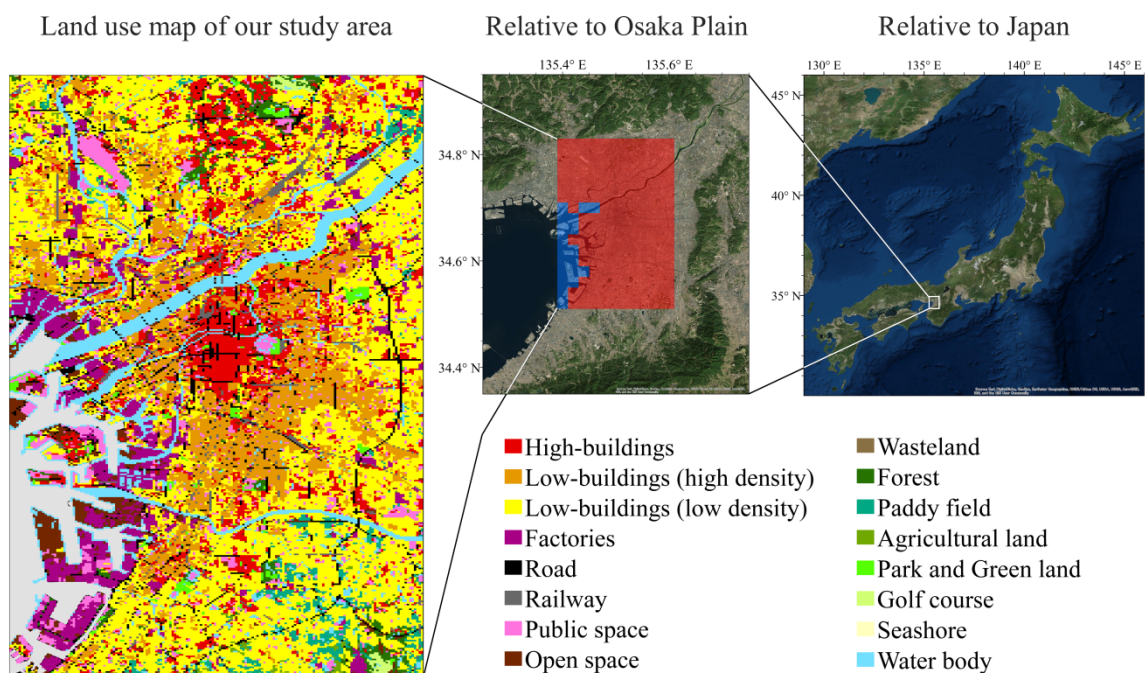
Fig. 1. Location map and land use of the study area (34.51°N–34.83°N, 135.39°E–135.61°E). In the middle figure, LST pixels used in the analysis are shown in red, whereas pixels with a percentage of water surface above 50% are shown in blue.

85   temperatures and land surface emissivities of bands 13, 14, and 15 (centered at 10.4, 11.2 and 12.4 μm, respectively)

86   of Himawari-8 in the thermal infrared region. The brightness temperature data of Himawari-8 were provided by the

87   Center for Environmental Remote Sensing, Chiba University, whereas the land surface emissivities were estimated

88   by a semi-empirical method based on the land cover information and NDVI (Yamamoto and Ishikawa, 2018b). LST

89   retrieval was limited to a clear-sky condition where the upward thermal infrared radiance from the land surface can

90   be observed by the Himawari-8 sensor. The spatial and temporal resolutions of the retrieved LST data were 0.02°

91   and 10 min, respectively. A total of 157 terrestrial pixels which have water surface percentage of less than 50% were

92   used in all pixels of the study area (Fig. 1). The satellite zenith angle in the study area ranges from 40.47°– 40.86°.

93   Therefore, all pixels used in the analysis were observed at approximately the same angle. The days when the diurnal

94   change of LST of the 157 pixels was retrieved (i.e., days with zero cloud cover) were chosen for focal analysis on

95   the temporal change characteristics of LST. The target season was summer. The presence of clouds was judged by a

96   cloud detection method employing Himawari-8's visible and infrared data (Yamamoto et al., 2018). The selection

97   period was the summer season, from July 2015 of the onset of the Himawari-8 operation to August 2018. The final

98   selected dates were August 12, 2016, July 19, 2018, and August 4, 2018.

99   The urban area land-use segmentation mesh data of national land numerical information provided by the Ministry

100   of Land, Infrastructure and Transport of Japan (http://nlftp.mlit.go.jp/ksj/gml/datalist/KsjTmplt-L03-b-u.html; see

101   Fig. 1) were used for investigating the relationship between LST and urban land use. The spatial resolution was 100

102   m; i.e., it was resolved with approximately 400 grid of land-use information per pixel of the LST data. Furthermore,

103   the SAT, wind direction, and wind speed data from the Automated Meteorological Data Acquisition System

104   (AMeDAS) operated by the Japan Meteorological Agency, were exploited for investigating the relationship between

105   LST and meteorological field. The observation points included Osaka, Toyonaka, Sakai, and Yao (see Figs. S1–S3)

106   at 10 min temporal resolution.

107   **2.2 Method of analysis**

108   The influence of urban spatial configuration and sea breeze on the temporal changes of LST, not the instantaneous

109   LST, was the highlight of this study. Such temporal changes were defined through a summary of the original diurnal

110   changes of LST using the principal component analysis (PCA). In other words, they were the principal temporal

111   change characteristics forming the diurnal changes of LST.

112   The temporal resolution of the LST data was 10 min, leading to a total of 144 LSTs retrieved for each pixel

113   throughout the day. As the PCA was applied, the diurnal changes of LST were converted into the diurnal changes of

114   the deviation by subtracting the daily mean LST of each pixel. The diurnal changes of the deviation of all pixels were

115   expressed as the following 157×144 matrix $\boldsymbol{dT}$:

$$\boldsymbol{dT} = \begin{pmatrix} dT_{1,1} & \cdots & dT_{1,144} \\ \vdots & \cdots & \vdots \\ dT_{157,1} & \cdots & dT_{157,144} \end{pmatrix} , \tag{1}$$

116   and the 144×144 variance-covariance matrix $\boldsymbol{V}$ of $\boldsymbol{dT}$ was calculated as follows:

$$\boldsymbol{V} = \begin{pmatrix} s_{1,1} & \cdots & s_{1,144} \\ \vdots & \cdots & \vdots \\ s_{144,1} & \cdots & s_{144,144} \end{pmatrix} , \tag{2}$$

117   where the variances and covariances contained in $\boldsymbol{V}$ were given by:

$$s_{ij} = s_{ji} = \frac{1}{157} \sum_{k=1}^{157} (dT_{ik} - \overline{dT_i})(dT_{jk} - \overline{dT_j}) , \tag{3}$$

118   where $\overline{dT_i}$ $(\overline{dT_j})$ is a column average of elements at time i (j) in $\boldsymbol{dT}$. By solving the eigenvalue problem for $\boldsymbol{V}$,

119   the eigenvalues $(\lambda_1, \ldots, k, \ldots, \lambda_{144})$ and the corresponding eigenvectors $\boldsymbol{a_k} = (a_{k1}, \ldots, a_{k144})$ were obtained.

Table 1. Eigenvalues and contribution ratios from PC1 to PC5 derived by the PCA on the three analysis days.

Principal Component	August 12, 2016		July 19, 2018		August 4, 2018	
	Eigenvalue	Contribution Ratio (%)	Eigenvalue	Contribution Ratio (%)	Eigenvalue	Contribution Ratio (%)
PC1	108.15	85.26	142.08	78.08	129.85	84.95
PC2	8.76	6.91	21.84	12.00	10.60	6.93
PC3	4.97	3.92	6.17	3.39	4.95	3.24
PC4	1.77	1.39	4.73	2.60	2.40	1.57
PC5	0.84	0.66	2.34	1.29	1.30	0.85

120   Therefore, the number of principal components (PCs) is 144. The 1×157 PC score of each PC was calculated as the

121   scalar product of dT and a_k. 157 PC scores were normalized for each PC. In this analysis, the PC score represents

122   the reflection degree of the temporal change characteristic represented by each PC in each pixel. The eigenvector

123   represents the weight corresponding to the LST deviation at each time in the calculation of the PC score.
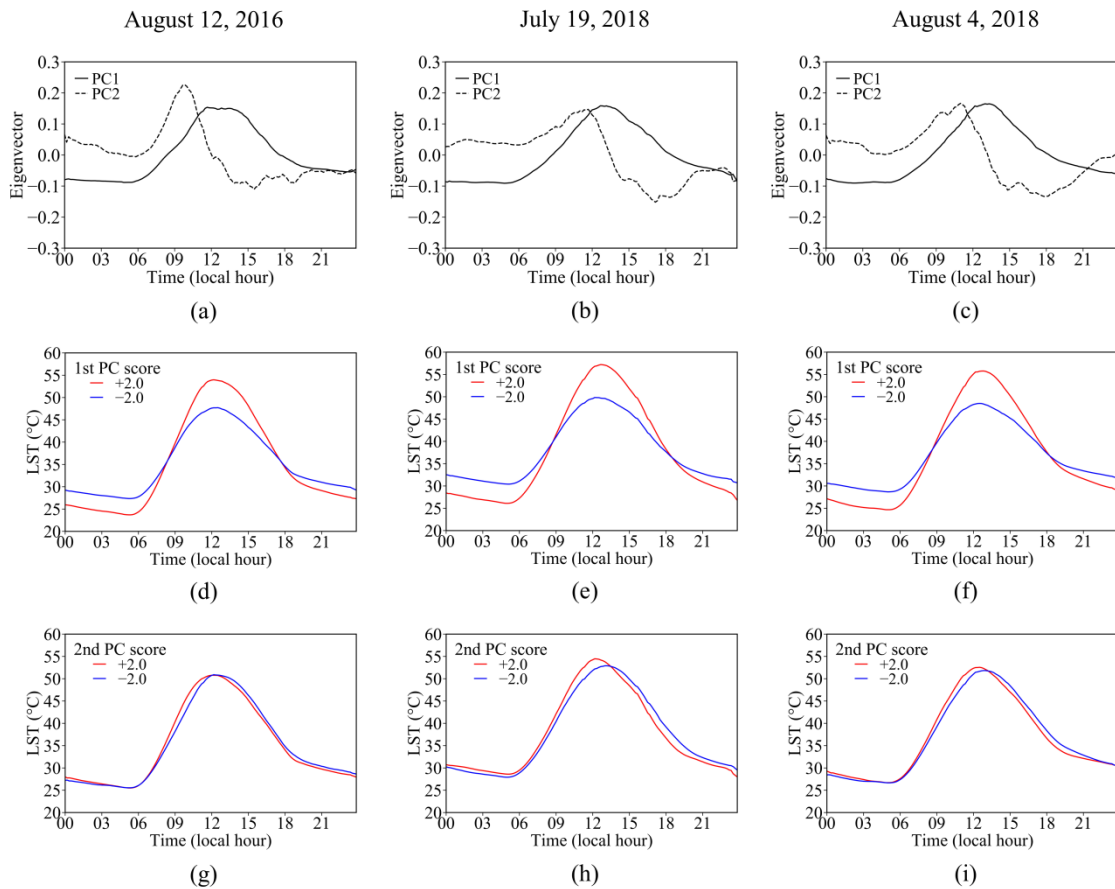
124

125

Fig. 2. (a)–(c) PC1 and PC2 eigenvectors f for the three analysis days. (d)–(f) Effect of PC1 on diurnal change of the average LST of the study area. (g)–(i) Effect of PC2 on diurnal change of the average LST of the study area.

3. PCA results

126

127   Table 1 shows the eigenvalues and contribution ratios from the first PC (PC1) to the fifth PC (PC5) derived by the

128   PCA. The contribution ratios of PC1 were dominant, and the cumulative contribution ratios of PC1 and PC2 were

129   more than 90% on all 3 days. In other words, the diurnal cycle of LST in a summer clear-sky day could be adequately

130   described by the temporal change characteristics represented by PC1 and PC2. This led to the investigation of the

131   influence of the urban spatial configuration and meteorological field on the temporal change characteristics of LST

132   represented by PC1 and PC2.

133   Figs. 2(a) to 2(c) show the eigenvectors of PC1 and PC2. The former had negative and positive components at

134   nighttime and daytime, respectively, on all 3 days, with the positive maximum value reached around noon. Note that

135   the temporal change characteristic represented by PC1 was emphasized around noon. Figs. 2(d) to 2(f) show the

136   responses of diurnal change of the average LST of 157 pixels in the study area when only the normalized PC score

137   of PC1 was changed by ± 2.0. For the average LST deviation of the study area, the PC scores from PC1 to PC144

138   were 0. Thus, by changing only the PC1 score, the temporal change characteristics represented by PC1 can be

139   emphasized. From Figs. 2(d) to 2(f), the amplitudes of the diurnal cycle were observed to vary with the variation of

140   the PC score on all 3 days, implying that PC1 represents the amplitude of the diurnal cycle on the clear-sky days.
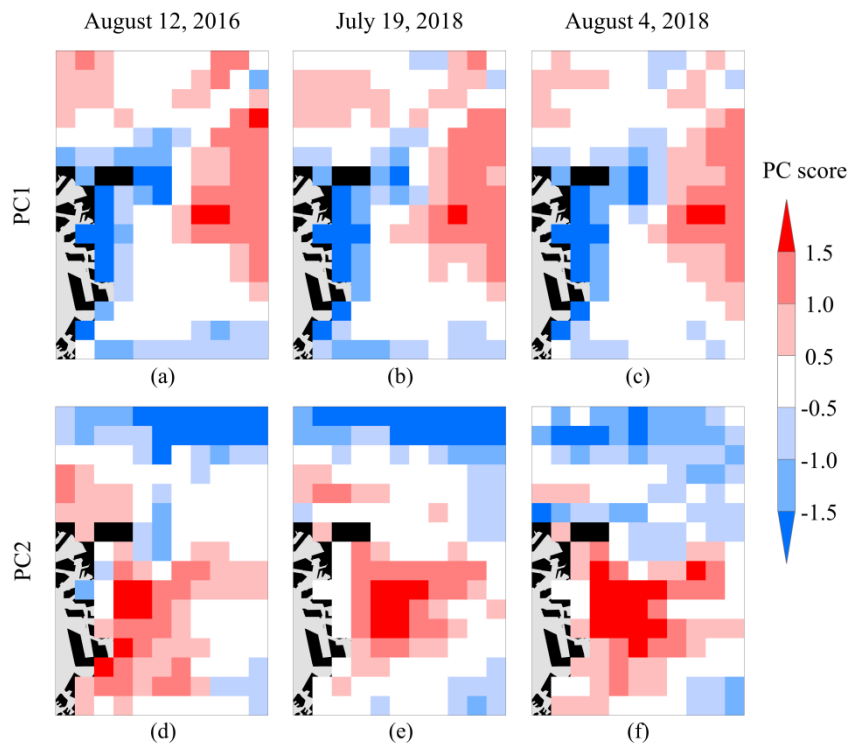

Fig. 3. Spatial distributions of the normalized PC scores of PC1 (a–c) and PC2 (d–f) derived by the PCA on the
three analysis days.

141 As shown in Figs. 2(a) to 2(c), the components of PC2 eigenvectors tended to be positive in the forenoon (i.e., the

142 time between midnight and around noon) and negative in the afternoon (i.e., the time between around noon and

143 midnight). The vector components took a positive maximum value from 9:00 to 12:00 when the temperature rise

144 became large, whereas they took a negative maximum value from 15:00 to 18:00 when the temperature drop was

145 large. Moreover, the components were close to 0 around noon when the vector components of PC1 took an extreme

146 value. Figs. 2(g) to 2(i) display a visualization of the temporal change characteristic represented by PC2, similar to

147 Figs. 2(d) to 2(f). These figures imply that PC2 represents the phase shifting by the waveform leaning

148 forward/backward and independent of the amplitude.

149 As described above, a large (small) PC1 score indicates that the amplitude of the diurnal cycle is relatively large

150 (small). A large (small) PC2 score indicates that the phase of the diurnal cycle is relatively advanced (delayed). Fig.

151 3 shows the spatial distributions of the scores of PC1 and PC2, with the former at a positive tendency in the inland

152 area and at a negative tendency in the coastal area. On the other hand, the spatial variability of the PC2 score tended

153 to be geographically opposite to that of PC1. Nevertheless, both score distributions were not diametrically opposite

154 and seemingly corresponding to land-use distribution. For example, the scores of both PCs were low in a pixel

155 occupied by high buildings (see Fig. 1), regardless of the area being coastal or inland.

156

4. Discussion

158 Fig. 4 shows the scatter diagrams of PC1 and PC2 scores for the three analysis days, with the addition of dominant

159 land-use type and coastal distance information. Moreover, in order to objectively classify the characteristics of the

160 distributions in Fig. 4, we performed cluster analysis (Ward's method) using the 1st and 2nd PC scores, coastal

161 distance (pixels) and proportions of high-buildings, low-buildings (high density), low-buildings (low density),

162 factories, vegetation, and water body of each pixel as input variables. These variables were standardized as pre-

163 processing. The clusters were classified with a threshold Euclidean distance of 10. Figs. S1 – S3 are the dendrograms

164 obtained by the cluster analysis, and Table 2 shows the characteristics of the obtained clusters for each analysis day.

165 The clusters consistently obtained on all analysis days were characterized as follows: pixels with a high proportion

166 of high-buildings (see (a) cluster1, (b) cluster4, and (c) cluster5 in Table 2); pixels with a high proportion of low-

167 buildings (high density) (see (a) cluster7, (b) cluster7, and (c) cluster2 in Table 2); coastal pixels with a high

168 proportion of low-buildings (low density) (see (a) cluster8, (b) cluster6, and (c) cluster4 in Table 2); inland pixels
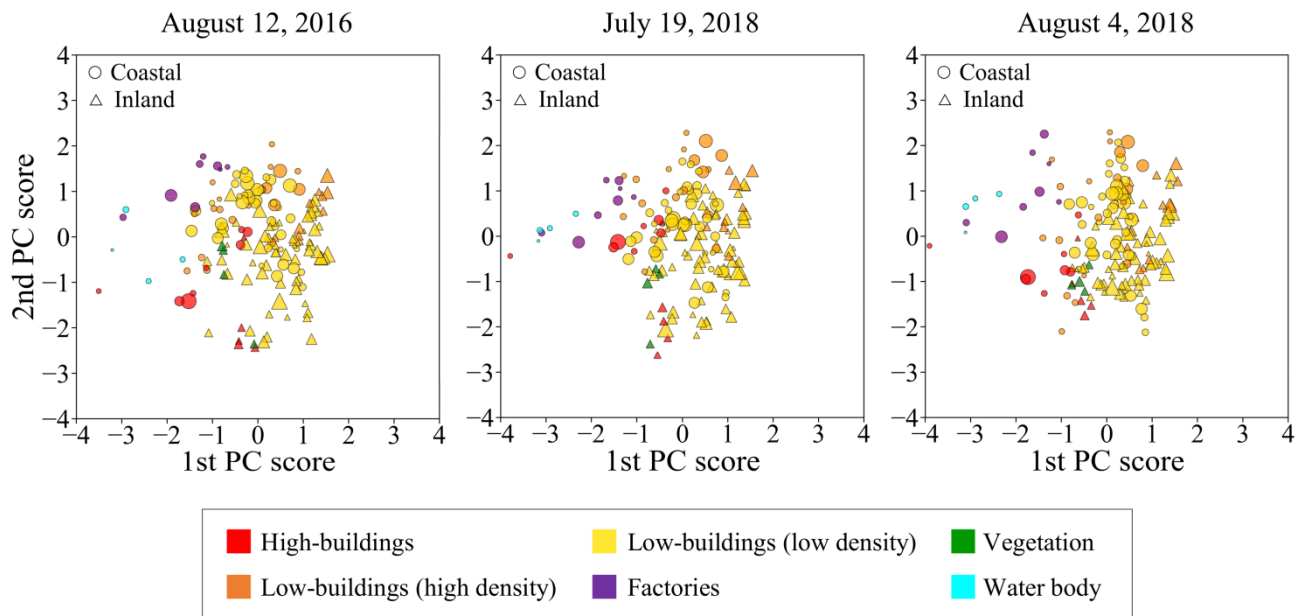
Fig. 4. Scatter diagrams between the PC1 and PC2 scores of the pixels for the three dates in the study area. Of all pixels for each date, half of the pixels close to the coast are indicated by circles as the coastal pixels, and half of the pixels far from the coast are indicated by triangles as the inland pixels. Each pixel is color coded according to land-use type with the highest occupancy, and the marker size corresponds to the occupancy rate.

169   with a high proportion of low-buildings (low density) (see (a) cluster4, (b) cluster2, and (c) cluster7 in Table 2);

170   coastal pixels with a high proportion of factories (see (a) cluster5, (b) cluster5, and (c) cluster1 in Table 2); inland

171   pixels with a high proportion of vegetation (see (a) cluster3, (b) cluster3, and (c) cluster6 in Table 2); pixels with a

172   high proportion of water body (see (a) cluster6, (b) cluster1, and (c) cluster3 in Table 2). Only on August 12, 2016,

173   pixels with a relatively close Euclidean distance from cluster1 but are located inland were classified as cluster2. This

174   section discusses the consistent or inconsistent characteristics of PC1 and PC2 in three analysis days in terms of the

175   land-sea breeze circulation and urban land use.

176   **4.1 Relationship between LST and sea breeze**

177   As shown in Fig. 4, coastal pixels (indicated by circles) tended to have a low PC1 score and a high PC2 score.

178   Conversely, inland pixels (indicated by triangles) tended to have a high PC1 score and a low PC2 score. Such

179   tendencies were aligned with the observation of Yamamoto and Ishikawa (2018a) who considered these to be the

180   results of land and sea breeze circulation, although concrete evidence of the relationship is yet to be found. The

181   variability of the land and sea breeze circulation was accounted herein through a more robust analysis of three

182   different meteorological cases.

Table 2. Clusters resulting from cluster analysis and their mean characteristics of the input variables on (a) August 12, 2016, (b) July 19, 2018, and (c) August 4, 2018.

(a) August 12, 2016

Cluster	1st PC score	2nd PC score	Coastal distance [pixels]	High-buildings [%]	Low-buildings (high density) [%]	Low-buildings (low density) [%]	Factories [%]	Vegetation [%]	Water body [%]
1	-1.25	-0.67	4.67	43.71	13.95	7.55	0.64	2.48	5.17
2	0.31	-1.98	8.74	27.53	2.42	42.80	1.44	10.14	2.03
3	-0.72	-0.56	8.58	3.09	0.24	46.07	3.09	33.68	4.78
4	0.71	-0.23	8.62	8.61	4.80	63.33	2.75	4.80	4.34
5	-1.17	1.36	2.29	2.25	2.87	10.18	40.19	1.47	16.31
6	-0.98	-0.24	5.26	11.28	10.32	20.93	9.41	1.32	27.05
7	0.78	0.64	6.63	11.74	47.51	22.68	0.66	1.97	1.73
8	-0.11	0.52	4.09	9.52	15.10	42.33	6.92	3.99	6.69

(b) July 19, 2018

Cluster	1st PC score	2nd PC score	Coastal distance [pixels]	High-buildings [%]	Low-buildings (high density) [%]	Low-buildings (low density) [%]	Factories [%]	Vegetation [%]	Water body [%]
1	0.11	-0.36	7.72	15.93	10.40	30.72	3.01	0.93	26.18
2	0.44	-0.40	7.50	11.49	5.36	57.66	2.46	5.89	4.38
3	-0.60	-0.94	8.74	3.01	0.26	43.82	3.34	35.31	4.88
4	-0.71	-1.03	6.65	50.54	3.46	13.53	0.02	10.11	3.33
5	-2.27	0.45	2.08	5.75	2.52	11.25	29.50	1.96	19.42
6	-0.10	0.73	3.34	6.84	23.63	34.22	9.78	1.92	7.64
7	0.65	0.87	6.65	14.48	46.78	19.46	0.63	1.86	1.92

(c) August 4, 2018

Cluster	1st PC score	2nd PC score	Coastal distance [pixels]	High-buildings [%]	Low-buildings (high density) [%]	Low-buildings (low density) [%]	Factories [%]	Vegetation [%]	Water body [%]
1	-2.27	0.82	2.08	5.75	2.52	11.25	29.50	1.96	19.42
2	0.65	0.60	6.58	13.63	48.23	19.51	0.58	1.90	1.77
3	-0.20	-0.93	5.49	11.17	18.56	27.99	7.17	1.10	19.42
4	0.05	0.85	4.28	8.89	13.47	47.55	5.68	4.61	5.65
5	-0.93	-1.14	6.65	50.54	3.46	13.53	0.02	10.11	3.33
6	-0.54	-0.73	8.91	2.96	0.05	37.10	4.68	40.43	6.00
7	0.56	-0.49	8.33	11.47	5.14	57.79	2.60	6.45	3.52

183   Fig. 5 shows the penetration time and duration of the sea breeze at each ground observation point for the 3 days.

184   Penetration time and end time of the sea breeze were judged on the basis of changes in wind direction/speed and

185   SAT. Thus, the westerly wind (270°±22.5°) at Sakai and Yao, and southwesterly wind (225°±22.5°) at Osaka and

186   Toyonaka were regarded as the sea breeze, respectively. The penetration time was defined as the time when the wind

187   speed increased, its direction continued for more than 30 min, and the SAT decreased within 30 min. The end time

188   was judged as the time when the wind speed decreased and the wind direction began to change in a direction other

189   than that of the sea breeze. More detailed wind direction/speed and SAT time-series changes are shown in Figs.

190   S4–S6.

191   Sea breeze causes reduction in both the SAT and the LST. Thus, the trend of the low PC1 score of coastal pixels

192   was thought to be due to the suppression of LST rise by a cool sea breeze, which reduced PC1's amplitude. Moreover,

193   the differences between the coastal and inland PC2 scores were thought as a result of the penetration time and duration

194   of the sea breeze. The sea breeze characteristics for the August 12, 2016, case showed the least amount of regional
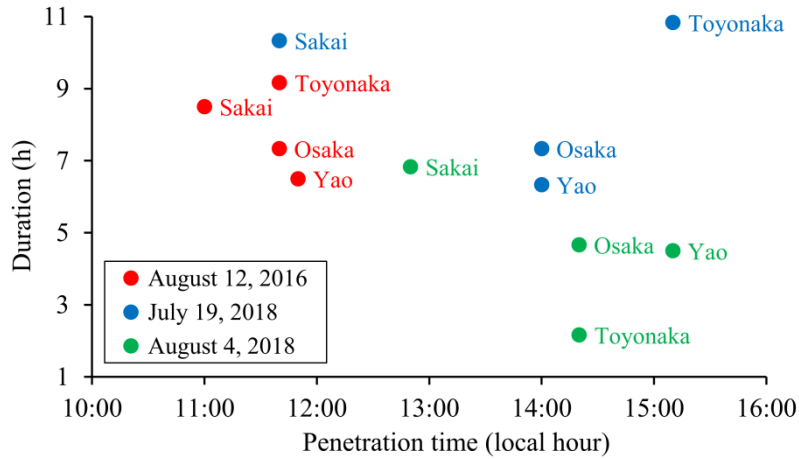
Fig. 5. Penetration time and duration of the sea breeze observed at the stations of AMeDAS in the study area on the three analysis dates.

195   variability compared with the other two cases (see Fig. 5). As shown in Fig. 2a, the components of PC2 eigenvector

196   on August 12, 2016, did not have a clearly defined minimum value in the afternoon. In other words, the leaning of

197   the wave on this day was affected by the heating rate in the morning rather than the cooling rate in the afternoon.

198   This result can be explained by the fact that not much regional difference occurred in the penetration time and duration

199   of the sea breeze. Thus, the cooling effect of the sea breeze without regional difference may have reduced the regional

200   difference of LST cooling rate during the afternoon.

201   For the other 2 days, regional differences in the penetration time were large (Fig. 5), especially on July 19, 2018,

202   whose duration was longer than on August 4, 2018. The components of PC2 eigenvectors in the afternoon on these

203   2 days took smaller minimum values than those on August 12, 2016, which can be attributed from the regional

204   difference in penetration time and duration of the sea breeze contrary to the case on August 12, 2016. In addition, the

205   duration on July 19, 2018, was long, potentially causing large regional difference in the degree of the LST drop. As

206   a result, PC2 contribution ratio may have become large (Table 1), and the PC2 score of the coastal pixels likewise

207   became large, as compared with those of the other 2 days (Fig. 4).

208   **4.2 Relationship between LST and urban land use**

209   As shown in Fig. 4 and Table 2, the pixels occupied by high-buildings, factories, vegetation, or bodies of water

210   tended to exhibit a low PC1 score, whereas that of pixels occupied by low-buildings (high/low density) tended to be

211   high. Such tendency could be attributed to the thermal inertia of the surface material. Thermal inertia is a thermal

212   and physical property indicating the degree of resistance to temperature change of a surface material (Sugawara and

213   Kondo, 1995; Haffner and Kidder, 1999; Zhan et al., 2012). As water surface has large thermal inertia, the amplitude

214   of the diurnal cycle at pixels occupied by the water bodies is small. In urban land-use areas, the amplitudes of the

215   diurnal cycle may reflect the thermal inertia of building roof and wall materials rather than the road materials since

216   the satellite zenith angle of Himawari-8 in the analysis area is about 40°. High-buildings and factories mainly consist

217   of concrete, glass and metal, which similarly show large thermal inertia. By contrast, low-buildings mainly consist

218   of wooden materials and slate roof that have small thermal inertia. Thus, differences in the building materials were

219   thought to have caused variation in the PC1 amplitude. A similar interpretation was made by previous studies using

220   polar-orbiting satellite/aircraft sensors, from the viewpoint of the thermal inertia or heat capacity of building materials

221   (e.g., Li et al., 2011; Tsunematsu et al., 2016). However, depending on the width among building clusters and street

222   orientation, more road surfaces are observed, and it is necessary to consider surface materials such as asphalt with

223   high thermal inertia. As shown in Table 2 (a) cluster5, (b) cluster5, and (c) cluster1, the pixels occupied by the

224   factories and water bodies may have been affected by the cooling effect of the sea breeze, being proximal to the coast.

225   Regarding the vegetated areas, transpiration was believed to have suppressed LST rise at daytime.

226   With regard to PC2, pixels occupied by the low-buildings (high density) tended to have high scores regardless of

227   the area as coastal and inland. The values of thermal inertia were thought to have varied from large to small, as the

228   land use changed from high-buildings, low-buildings (high density), and to low-buildings (low density) with the

229   decrease in concrete buildings and the increase in wooden buildings (Haffner and Kidder, 1999; Tsunematsu et al.,

230   2016). The larger the thermal inertia, the smaller was the amplitude (i.e., lower PC1 score) and the later the phase

231   (i.e., higher PC2 score). Nonetheless, only those pixels occupied by the low-buildings (high density) were biased to

232   the first quadrant in Fig. 4 (i.e., high PC1 and PC2 scores, shown in Table 2 (a) cluster7, (b) cluster7, and (c) cluster2).

233   This possibly be because more road surfaces with high thermal inertia have been observed in low-buildings (low

234   density). In addition, differences in surface roughness between high/low building densities may have different heat

235   balance processes in the diurnal cycle on the clear-sky days.

236   The shadows of buildings during the daytime suppress the temperature rise of the land surface and cause a decrease

237   in the amplitude of the diurnal cycle. Depending on the street orientations, the timing affected by the shadows may

238   vary, which may change the PC2 score. The shadow effects are considered to have been most significant in the high-

239   buildings, which have high building height and large variations of the building height. The shadow effects also vary

240   with the number of buildings and the width between buildings. It is challenging to discuss which is more affected by

241   shadows, the low-buildings (high density) with many buildings or the low-buildings (low density) with wide spaces

Fig. 6 shows the diurnal LST changes calculated using average PC1 and PC2 scores and daily mean LST of the

coastal pixels occupied by high-buildings, low-buildings (high density), and low-buildings (low density). LST at

nighttime was lower in the order of high-buildings, low-buildings (high density), and low-buildings (low density),

which could be due to the thermal inertia of the building materials as described above. However, the order during

daytime was not reversed of that during nighttime, and the low-buildings (high density) had the highest LST, implying

an increase in internal reflections of solar and infrared radiations, along with wind speed reduction between the

buildings as their density increased. More complex internal reflection of the radiations implies higher absorptivity

and thereby causes higher heating rate at daytime. Moreover, at a location where variation in building height was

small and that for building density was high, the wind above the group of buildings hardly blew into spaces between

the buildings (Hagishima et al., 2004). The convective heat transfer between the surface within street canyons (mainly

building walls and roads) and the atmosphere near it decreases under weak wind conditions. The LST retrieved from

Himawari-8 in the analysis area reflects the surface temperatures of more building roofs and walls in the street

canyons as the building density increases. Thus, these effects in radiation and wind fields may have resulted in a

larger rate of LST increase in the morning, and the waveform of the diurnal change leaned forward (i.e., the PC2

score increased) in the pixels occupied by low-buildings (high density).

LST differences between low-buildings (high density) and low-buildings (low density) shown in Fig. 6 may also

be due to differences in vegetation cover since vegetation reduces daytime and nighttime LST by transpiration.
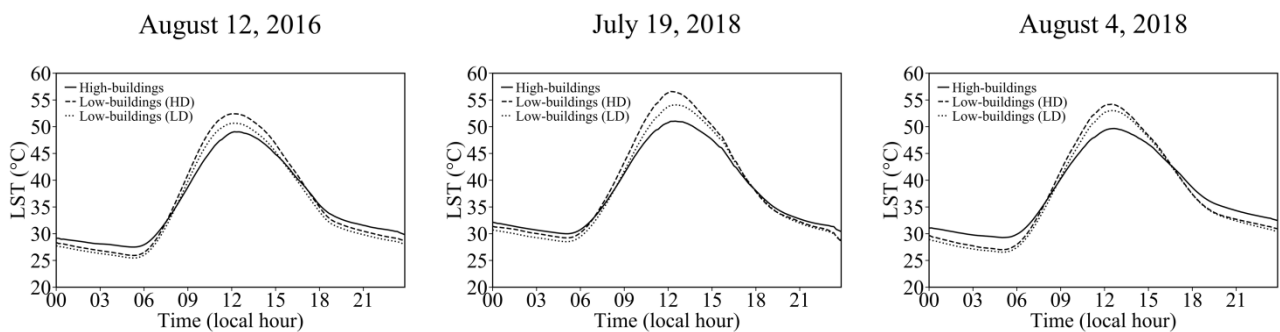

Fig. 6. Diurnal LST changes calculated with average PC1 and PC2 scores and daily mean LST of the coastal
pixels where occupancy rate of high-buildings, low-buildings (high density), and low-buildings (low density) are
higher than 70%. The solid, dashed, and dotted lines show the diurnal LST changes of high-buildings, low-
buildings (high density), and low-buildings (low density), respectively.

However, the mean proportions of vegetation class of pixels used in Fig. 6 were 1.07% for low-buildings (high density) and 3.28% for low-buildings (low density). The mean normalized difference vegetation index (NDVI) values on three analysis days were 0.30, 0.29, and 0.35 for low-buildings (high density), 0.32, 0.29, and 0.34 for low-buildings (low density). These small differences in vegetation cover are unlikely to have a significant effect on the diurnal LST changes shown in Fig. 6.

The difference in the surface material may also be a cause of LST differences between low-buildings (high density) and low-buildings (low density) shown in Fig. 6. In Japan, as distance to the city center decreases the proportion of concrete buildings increases whilst that of wood buildings decreases (Tsunematsu et al., 2016). The trend suggests that the effective thermal inertia is greater in the low-buildings (high density), but this is inconsistent with the larger amplitude of the low-buildings (high density) shown in Fig. 6. Besides, if the building materials in low-buildings (high density) were the same as those in low-buildings (low density), surface in low-buildings (high density) is covered by more roofs and walls (e.g., slate and wooden materials) and fewer roads (e.g., asphalt and concrete) compared with that in low-buildings (low density). In this case, the effective thermal inertia of the low-buildings (high density) is smaller than that of the low-buildings (low density), so the temperature should drop significantly during nighttime. This is also inconsistent with the nighttime LST shown in Fig. 6. Since the spatial resolution of Himawari-8 is low, it is challenging to discuss the relationship between a temporal LST change and surface materials in detail. However, it is difficult to interpret the results showing that the high-density areas of low-buildings were the hottest during the daytime, based solely on the thermal inertia of the surface materials.

5. Conclusions

This study exploited the high spatiotemporal resolution of Himawari-8 sensor for investigation of the influence of sea breeze and urban spatial configuration on the temporal changes of LST. The study area was an urban area of Osaka Plain, Japan, for target clear-sky days in midsummer. Temporal changes of the LST were defined as the principal temporal change characteristics forming the diurnal changes of LST, extracted via the PCA. The extracted characteristics included the amplitude and phase (waveform leaning) of the diurnal cycle, whose spatial variabilities were investigated using ground-based meteorological observation and land-use data of the study area.

As for the relationship with meteorological data, a reduction of the diurnal range and a forward-leaning of the waveform corresponding to the penetration time and duration of the sea breeze were observed, which suggests the

289 importance of considering the effect of land and sea breeze circulation when observing LST in coastal cities. The

290 eigenvalues (contribution ratio) and scores of PC2 have a potential application in assessing the effects of sea breeze

291 on LST and urban heat island patterns. Note that on cloudy days or in the winter season, the diurnal changes of LST

292 are small, and the characteristics of the land-sea breeze circulation are different from those on summer clear-sky

293 days. On such days, different temporal change characteristics from those in this analysis are expected.

294   As for the relationship with land-use data, the variations of PC1 and PC2 scores were confirmed to correspond to

295 the thermal inertia of the building materials, which is consistent with previous studies. Furthermore, pixels occupied

296 by the low-buildings (high density) yielded high scores for both PC1 and PC2, regardless of the area as coastal and

297 inland. At daytime, low-buildings (high density) tended to exhibit higher LST than high-buildings and low-buildings

298 (low density), which suggests the impact of building density on diurnal LST change. The findings of this study

299 provide new facts on the relationship between LST and urban spatial configuration, as has been suggested in previous

300 studies (Li et al., 2011; Connors et al., 2013). Furthermore, such findings contribute to a deeper understanding of the

301 hot environment. The combined knowledge of a spatial LST pattern derived from an aircraft or polar-orbiting satellite

302 and the diurnal LST patterns, including the effects of building density and sea breeze, derived from a new-generation

303 geostationary satellite, would help urban planners mitigate its deterioration due to urbanization. For example,

304 applying the presented analysis method to the rapidly urbanizing Asia-Megacities would contribute to improve the

305 thermal environment measures of each city.

306

307 **Acknowledgments**

310

311 **Declarations of interest**: none.

312

313 **References**

314 Budd, G.M., 2008. Wet-bulb globe temperature (WBGT)-its history and its limitations. J. Sci. Med. Sport 11, 20–32.

315   https://doi.org/10.1016/j.jsams.2007.07.003

316 Connors, J.P., Galletti, C.S., Chow, W.T.L., 2013. Landscape configuration and urban heat island effects: Assessing the

317   relationship between landscape characteristics and land surface temperature in Phoenix, Arizona. Landsc. Ecol. 28,

318   271–283. https://doi.org/10.1007/s10980-012-9833-1

319 Hafner, J., and Kidder, S. Q., 1999. Urban heat island modeling in conjunction with satellite-derived surface/soil

320   parameters. Journal of Applied Meteorology, 38, 448–465.

321 Hagishima, A., Tanimoto, J., Narita, K., 2004. Review of the former researches on the convective heat transfer

322   coefficient of urban surfaces. J. Japan Soc. Hydrol. Water Resour. 17, 536–554.

323 Honjo, T., Tsunematsu, N., Yokoyama, H., 2017. Urban climate analysis of urban surface temperature change using

324   structure- from-motion thermal mosaicing. Urban Clim. 20, 135–147. https://doi.org/10.1016/j.uclim.2017.04.004

325 Japan Fire and Disaster Management Agency, 2018. The emergency conveyance situation due to heat stroke of 2018

326   (May to September), (17 pp.) (in Japanese).

327 Japan Statistics Bureau, 2019. Statistical observations of prefectures 2019, (164 pp.) (in Japanese).

328 Jendritzky, G., De Dear, R., Havenith, G., 2012. UTCI—Why another thermal index? Int. J. Biometeorol. 56, 421–428.

329   https://doi.org/10.1007/s00484-011-0513-7

330 Kim, Y.-H., Baik, J.-J., 2005. Spatial and temporal structure of the urban heat island in Seoul. J. Appl. Meteorol. 44,

331   591–605. https://doi.org/10.1175/JAM2226.1

332 Kusaka, H., Hara, M., Takane, Y., 2012. Urban climate projection by the WRF model at 3-km horizontal grid increment:

333   Dynamical downscaling and predicting heat stress in the 2070's August for Tokyo, Osaka, and Nagoya

334   metropolises. J. Meteorol. Soc. Japan. Ser. II 90B, 47–63. https://doi.org/10.2151/jmsj.2012-B04

335 Li, J., Song, C., Cao, L., Zhu, F., Meng, X., Wu, J., 2011. Impacts of landscape structure on surface urban heat islands: A

336   case study of Shanghai, China. Remote Sens. Environ. 115, 3249–3263. https://doi.org/10.1016/j.rse.2011.07.008

337 Li, J., Wang, X., Wang, X., Ma, W., Zhang, H., 2009. Remote sensing evaluation of urban heat island and its spatial

338   pattern of the Shanghai metropolitan area, China. Ecol. Complex. 6, 413–420.

339   https://doi.org/10.1016/j.ecocom.2009.02.002

340 Memon, R.A., Leung, D.Y.C., Liu, C.H., 2009. An investigation of urban heat island intensity (UHII) as an indicator of

341   urban heating. Atmos. Res. 94, 491–500. https://doi.org/10.1016/j.atmosres.2009.07.006

342 Oku, Y., Masumoto, K., 2014. An observational study of the difference on urban heat islands between summer and

343   winter in Osaka city. J. Heat Isl. Inst. Int. 9, 1–12 (in Japanese with English abstract).

344 Saitoh, T.S., Shimada, T., Hoshi, H., 1996. Modeling and simulation of the Tokyo urban heat island. Atmos. Environ. 30,

345   3431–3442.

346   Seino, N., Aoyagi, T., Tsuguti, H., 2018. Numerical simulation of urban impact on precipitation in Tokyo: How does
347   urban temperature rise affect precipitation? Urban Clim. 23, 8–35. https://doi.org/10.1016/j.uclim.2016.11.007

348   Sugawara, H., Kondo, J., 1995. Sensitivity test of urban surface temperature. Tenki 42, 813–818 (in Japanese).

349   Suzuki, T., Iizuka, Y., 2009. Diurnal temperature changing patterns of Tokyo according to season and weather. Tenki 56,
350   627–635 (in Japanese).

351   Tsunematsu, N., Yokoyama, H., Honjo, T., Ichihashi, A., Ando, H., Shigyo, N., 2016. Relationship between land use
352   variations and spatiotemporal changes in amounts of thermal infrared energy emitted from urban surfaces in
353   downtown Tokyo on hot summer days. Urban Clim. 17, 67–79. https://doi.org/10.1016/j.uclim.2016.03.002

354   Tzavali, A., Paravantis, J.P., Mihalakakou, G., Fotiadi, A., Stigka, E., 2015. Urban heat island intensity: A literature
355   review. Fresenius Environ. Bull. 24, 4537–4554.

356   Weng, Q., 2009. Thermal infrared remote sensing for urban climate and environmental studies: Methods, applications,
357   and trends. ISPRS J. Photogramm. Remote Sens. 64, 335–344. https://doi.org/10.1016/j.isprsjprs.2009.03.007

358   Xu, L.Y., Xie, X.D., Li, S., 2013. Correlation analysis of the urban heat island effect and the spatial and temporal
359   distribution of atmospheric particulates using TM images in Beijing. Environ. Pollut. 178, 102–114.
360   https://doi.org/10.1016/j.envpol.2013.03.006

361   Yamamoto, Y., Ishikawa, H., 2018a. Spatiotemporal variability characteristics of clear-sky land surface temperature in
362   urban areas of Japan observed by Himawari-8. Sola 14, 179–184. https://doi.org/10.2151/sola.2018-032

363   Yamamoto, Y., Ishikawa, H., 2018b. Thermal land surface emissivity for retrieving land surface temperature from
364   Himawari-8. J. Meteorol. Soc. Japan 96B, 43−58. https://doi.org/10.2151/jmsj.2018-004

365   Yamamoto, Y., Ishikawa, H., Oku, Y., Hu, Z., 2018. An algorithm for land surface temperature retrieval using three
366   thermal infrared bands of Himawari-8. J. Meteorol. Soc. Japan 96B, 59−76. https://doi.org/10.2151/jmsj.2018-005

367   Zhan, W., Chen, Y., Voogt, J.A., Zhou, J., Wang, J., Ma, W., Liu W., 2012. Assessment of thermal anisotropy on remote
368   estimation of urban thermal inertia. Remote Sens. Environ. 123, 12–24.

Supplementary materials

Influence of urban spatial configuration and sea breeze on

land surface temperature on summer clear-sky days

Yuhei Yamamoto[1] and Hirohiko Ishikawa[1]

[1]*Disaster Prevention Research Institute, Kyoto University, Kyoto, Japan.*

Corresponding author: Yuhei Yamamoto

*Present address: Center for Environmental Remote Sensing, Chiba University, 1-33 Yayoi-cho, Inage-ku, Chiba-shi, Japan.

E-mail: yamamoto_y@storm.dpri.kyoto-u.ac.jp

Contents of this file
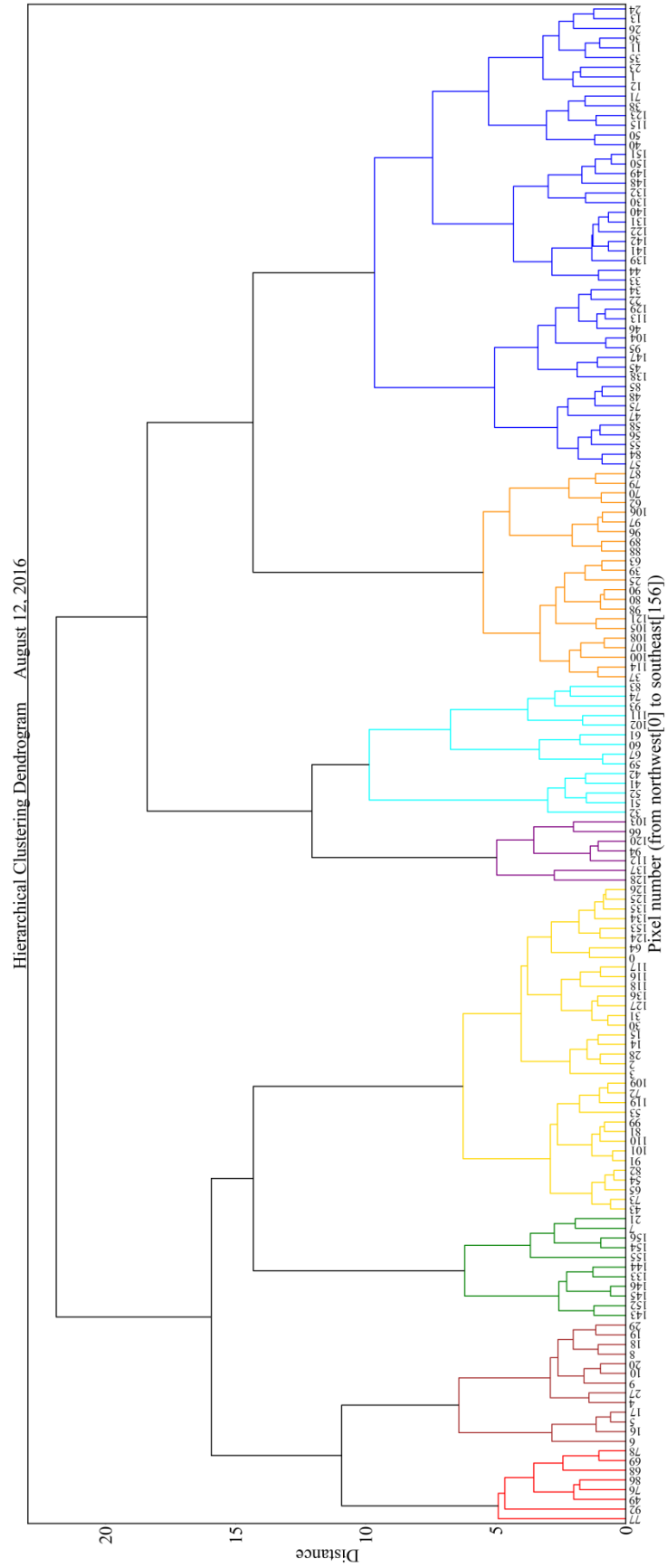
Fig. S1. Dendrograms obtained by the cluster analysis (Ward's method) on August 12, 2016. The horizontal axis represents the pixel number, and the vertical axis represents the Euclidean distance.
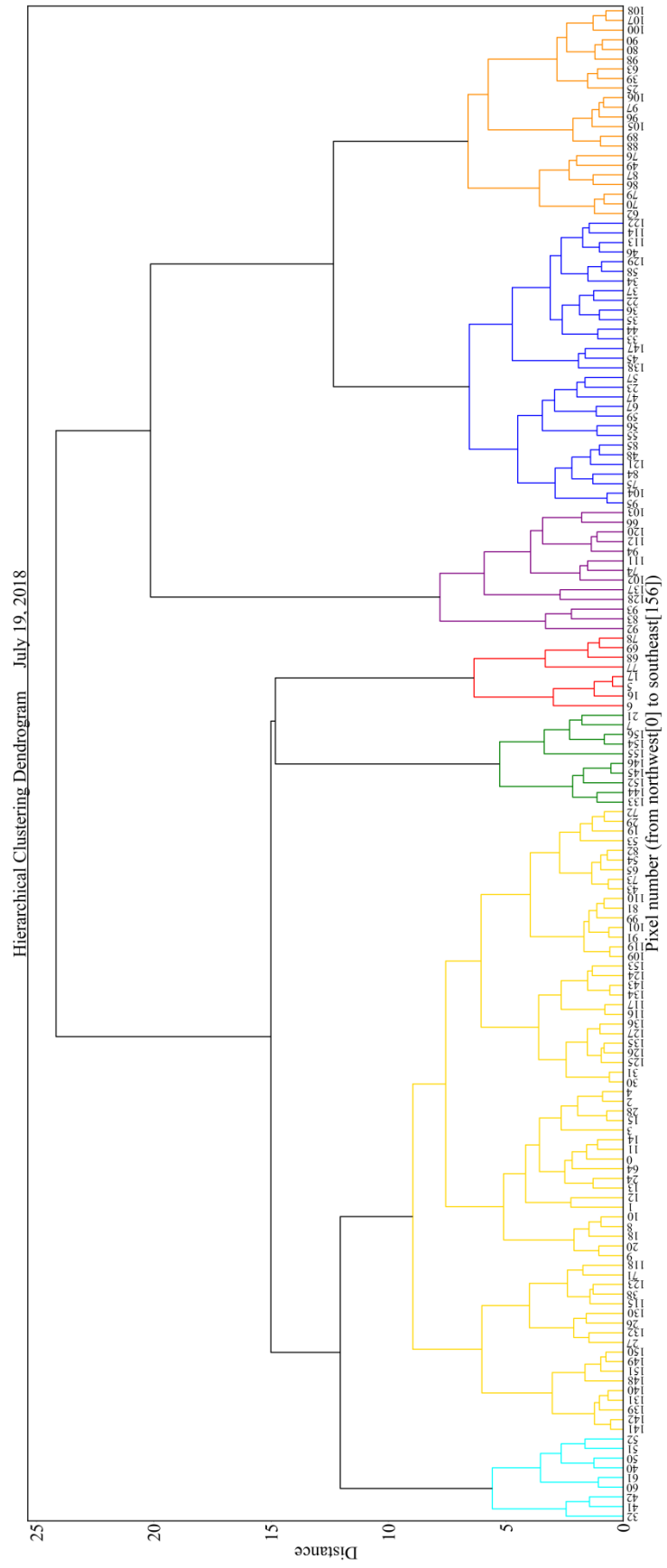
Hierarchical Clustering Dendrogram   July 19, 2018

Distance

Pixel number (from northwest[0] to southeast[156])

Fig. S2. Similar to Fig. S4, but for July 19, 2018.

3
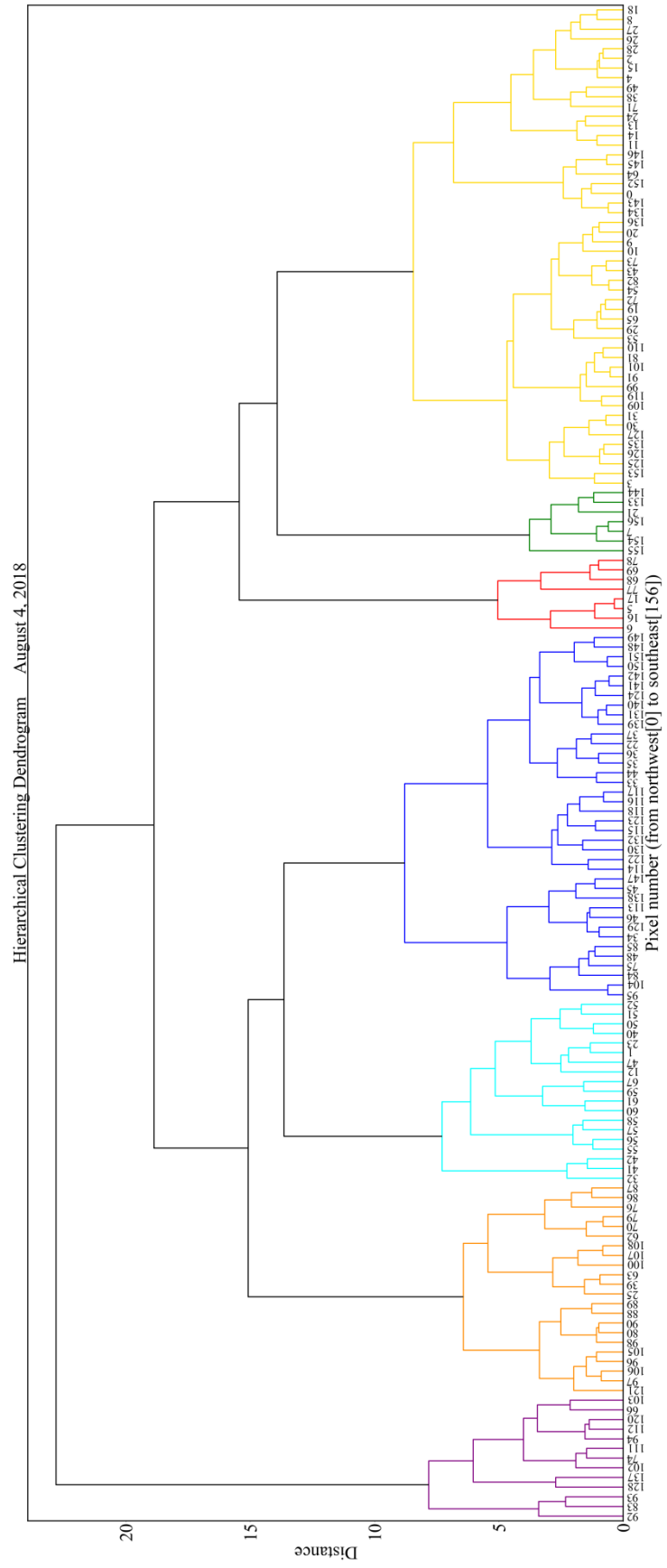
Fig. S3. Similar to Fig. S4, but for August 4, 2018.

4
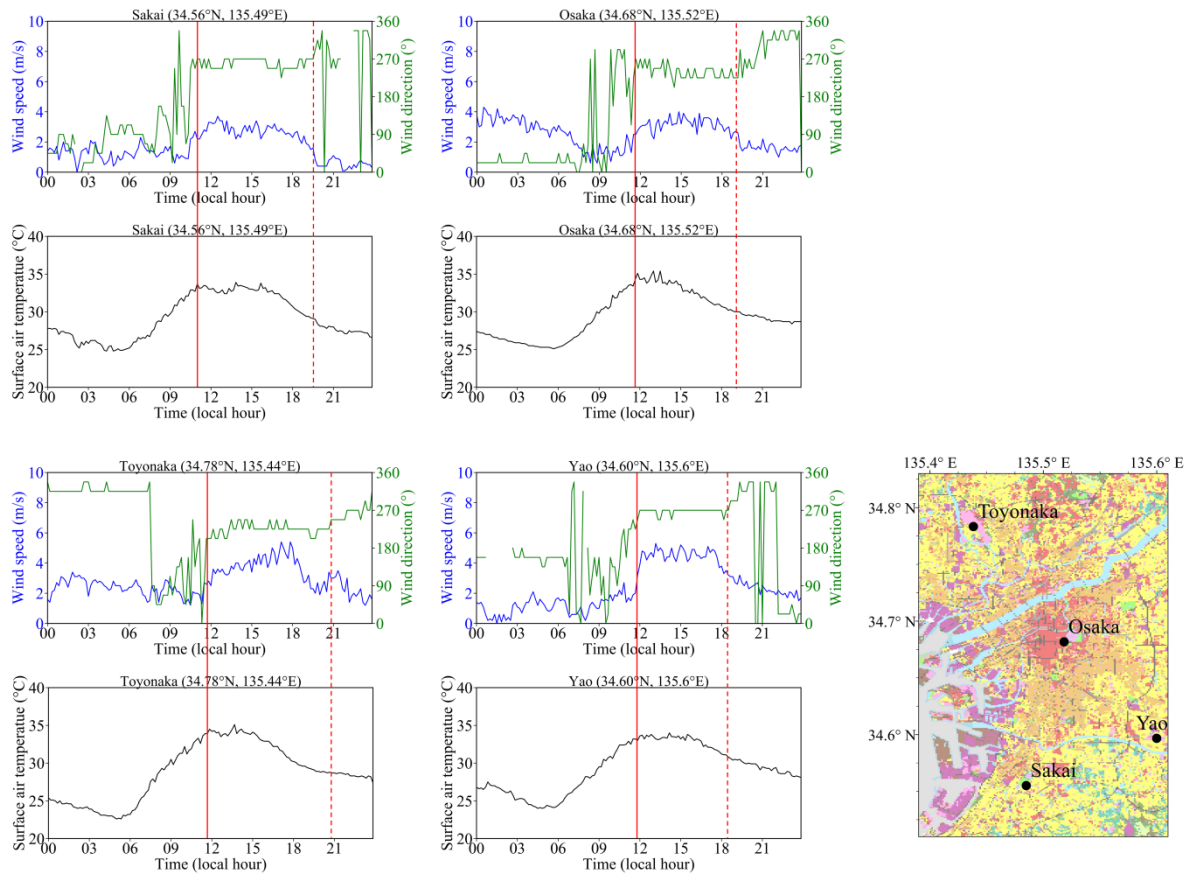
Fig. S4. Time series data of wind speed/direction and SAT observed at the stations of AMeDAS in the study area on August 12, 2016. The lower right figure shows the position of each observation point in the study area. The red solid lines indicate penetration times of the sea breeze roughly judged by changes in wind direction, increase in wind speed, and decrease in SAT. The end times of the sea breeze judged by the change in wind direction and wind speed are indicated by a red dashed line.
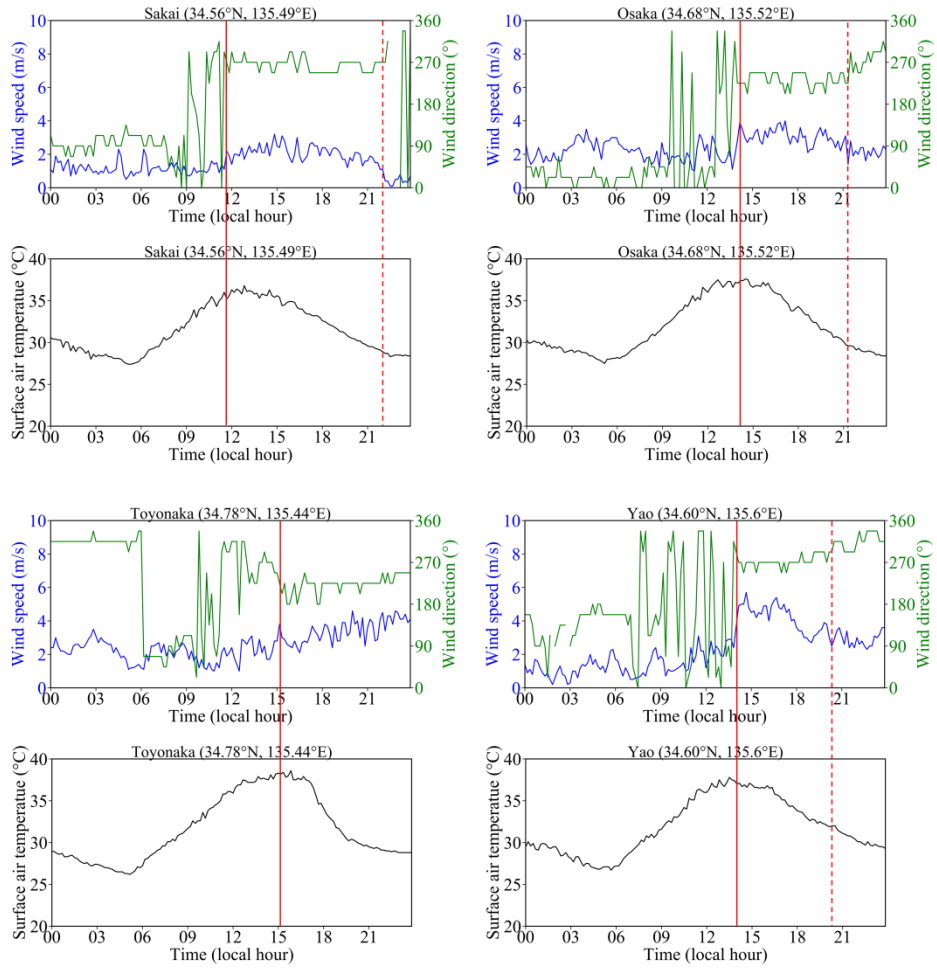
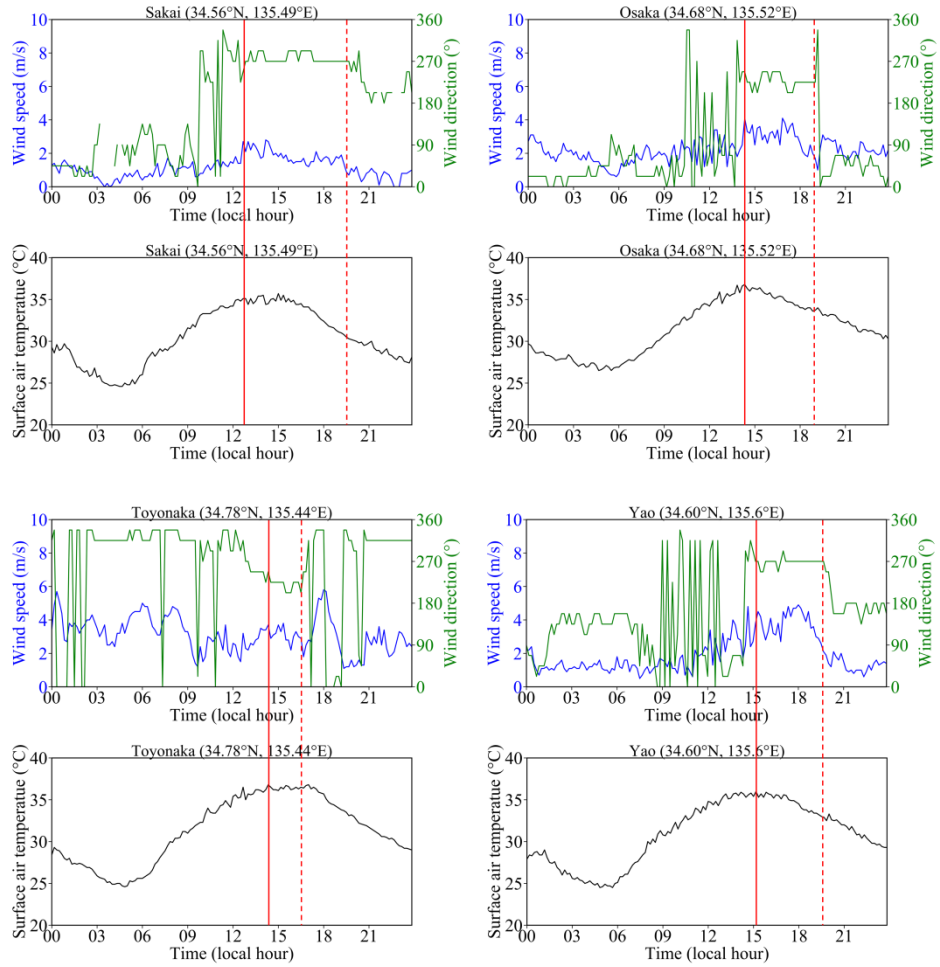Fig. S5. Similar to Fig. S1, but for July 19, 2018.

Fig. S6. Similar to Fig. S1, but for August 4, 2018.

Declaration of interests

☒ The authors declare that they have no known competing financial interests or personal relationships that could have appeared to influence the work reported in this paper.

☒The authors declare the following financial interests/personal relationships which may be considered as potential competing interests:

Declarations of interest: none

CRediT author statement

Yuhei Yamamoto: Conceptualization, Data curation, Formal analysis, Investigation, Methodology, Project administration, Software, Validation, Visualization, Writing - original draft, Writing - review & editing.

Hirohiko Ishikawa: Funding acquisition, Resources, Supervision

Urban Climate

Conflict of interest declaration and author agreement form

Title of Paper: Influence of urban spatial configuration and local meteorological field on land surface temperature on summer clear-sky days

1) We wish to confirm that there are no known conflicts of interest associated with this publication and there has been no significant financial support for this work that could have influenced its outcome.

2) We confirm that the manuscript has been read and approved by all named authors and that there are no other persons who satisfied the criteria for authorship but are not listed. We further confirm that the order of authors listed in the manuscript has been approved by all of us.

3) We confirm that neither the entire paper nor any of its content has been submitted, published, or accepted by another journal. The paper will not be submitted elsewhere if accepted for publication in the journal.

4) We confirm that we have given due consideration to the protection of intellectual property associated with this work and that there are no impediments to publication, including the timing of publication, with respect to intellectual property. In so doing we confirm that we have followed the regulations of our institutions concerning intellectual property.

5) We understand that the Corresponding Author is the sole contact for the Editorial process (including Editorial Manager and direct communications with the office). He is responsible for communicating with the other authors about progress, submissions of revisions and final approval of proofs.

Signed by all authors as follows:

Print name	Author signature	Date
Yuhei Yamamoto	Yuhei Yamamoto	April 5, 2019
Hirohiko Ishikawa	H. Ishikawa	April 5, 2019